

NOTICE

THIS DOCUMENT HAS BEEN REPRODUCED FROM
MICROFICHE. ALTHOUGH IT IS RECOGNIZED THAT
CERTAIN PORTIONS ARE ILLEGIBLE, IT IS BEING RELEASED
IN THE INTEREST OF MAKING AVAILABLE AS MUCH
INFORMATION AS POSSIBLE

NT
NASA Technical Memorandum 81637

(NASA-TM-81637) FULL POTENTIAL SOLUTION OF
TRANSONIC QUASI-3-D FLOW THROUGH A CASCADE
USING ARTIFICIAL COMPRESSIBILITY (NASA)
40 p HC A03/MF A01

N81-14980

CSSL 01A

Unclass

G3/02 29696

Full Potential Solution of Transonic Quasi-3-D Flow Through A Cascade Using Artificial Compressibility

C. Farrell and J. Adamczyk
*Lewis Research Center
Cleveland, Ohio*



Prepared for the
Twenty-sixth Annual International Gas Turbine Conference
sponsored by the American Society of Mechanical Engineers
Houston, Texas, March 8-12, 1981

NASA

FULL POTENTIAL SOLUTION OF TRANSONIC QUASI-3-D FLOW THROUGH
A CASCADE USING ARTIFICIAL COMPRESSIBILITY

C. Farrell and J. Adamczyk

National Aeronautics and Space Administration

Lewis Research Center

Cleveland, Ohio 44135

ABSTRACT

E-574

A reliable method is presented for calculating the flowfield about a cascade of arbitrary 2-D airfoils. The method approximates the three-dimensional flow in a turbomachinery blade row by correcting for streamtube convergence and radius change in the throughflow direction. The method is a fully conservative solution of the full potential equation incorporating the finite volume technique on a body-fitted periodic mesh, with an artificial density imposed in the transonic region to insure stability and the capture of shock waves. Comparison of results for several supercritical blades shows good agreement with their hodograph solutions. Other calculations for these profiles as well as standard NACA blade sections indicate that this is a useful scheme for analyzing both the design and off-design performance of turbomachinery blading.

INTRODUCTION

Some very useful tools for the study of transonic flows have been developed during the last few years. Conservative schemes, finite volume, and artificial density have all contributed to accelerating progress in this area. Each has been applied to the analysis of external flow over isolated airfoils in two and three dimensions with promising results.

In the area of internal flows the need to design lighter, more efficient turbomachine components has led to consideration of machines with

fewer stages, each with blades capable of higher speeds and higher loading. As speeds increase, the numerical problems inherent in the transonic regime have to be resolved. These include the calculation of imbedded shock discontinuities and the dual nature of the governing equations, which are elliptic in the subcritical flow regions but become hyperbolic for supersonic zones. The development of supercritical blade design has eliminated some of these difficulties by returning to the hodograph plane and explicitly designing blades that will be shock free. However, unlike the case of external wing aerodynamics, undesirable off-design conditions can develop much faster in turbomachinery flows and are not readily controlled or easily corrected. For these reasons the study of off-design conditions (high incidence, shocks, etc.) will remain a major requirement for internal flows. In addition, the periodic nature of the geometry for turbomachine components adds another degree of complexity which contributes to the importance of grid generation as another area of study in its own right.

The present analysis combines some of the most promising transonic analysis techniques to calculate the flowfield surrounding a cascade of airfoils. The full potential equation in conservative form has been discretized at each point on a body-fitted periodic mesh and a mass balance calculated through the finite volume surrounding the point. Each local volume is corrected in the third dimension for any change in streamtube thickness along the streamtube. Each is also corrected in the tangential $y(r\theta)$ direction due to any change in the radial position of the streamtube from upstream to downstream. The final result is a tridiagonal matrix formulation involving potential corrections at each grid point as the unknowns. The right hand side of each equation is equal to the net mass

flux through a volume. The resulting system of equations is solved along each grid line by an SLOR procedure. At points where the Mach number exceeds unity, the density at the forward (sweeping) edge of the volume is replaced by an artificial density as suggested in reference 1. This artificial density is a function of the real gas density and its streamwise derivative.

In the following sections, two body-fitted mesh generators that were incorporated into the resulting computer code are discussed. The full potential equation in finite difference form is also reviewed along with details on the solution method employed. Subsonic and transonic calculations using this method on a NACA0012 profile are compared to other computational procedures. Results for several supercritical blade designs of Sanz are compared to their hodograph solutions. The quasi-3-D capabilities of the method are compared to results from reference 9.

MESH GENERATION

The flowfield is discretized using a body-fitted, periodic O-type mesh. Two techniques were developed to generate computational grids. The original grid generation technique, referred to here as the interpolation scheme, is near-orthogonal and combines the use of analytical functions, interpolations, and simple stretchings. No numerical system must be solved for the generation of the grid. The second method, an electrostatic analog was developed when the grids generated by the interpolation scheme were found to be unsatisfactory for cascades of high camber, thickness, and solidity.

Interpolation Scheme

A summary of this procedure is shown in figure 1. As suggested in reference 2, beginning with the orthogonal, computational plane,

$$-K' < \xi < +K' \quad 0 < \eta < K$$

the transformation to a physical (x,y) plane as described by the Jacobian elliptic functions sn , cn , and $\text{dn}(\xi)$, is given as:

$$x = \frac{s}{2\pi} \left[\ln \frac{1}{k} - 2 \ln \frac{\Gamma}{\Gamma'} \right]$$

$$y = \frac{s\Omega}{\pi}$$

where

$$k = e^{-\frac{\pi c}{s \cos \lambda}}$$

and

λ = stagger angle

s = blade spacing

c = chord

$$\Gamma = \left[\left(\text{sn}(\eta, m) \cdot \text{dn}(\xi, m_1) \right)^2 + \left(\text{cn}(\eta, m) \cdot \text{dn}(\eta, m) \cdot \text{sn}(\xi, m_1) \cdot \text{cn}(\xi, m_1) \right)^2 \right]^{1/2}$$

$$\Gamma = \text{cn}^2(\xi, m_1) + m \cdot \text{sn}^2(\eta, m) \cdot \text{sn}^2(\xi, m_1)$$

$$\Omega = \tan^{-1} \left\{ \frac{\text{cn}(\eta, m) \cdot \text{dn}(\eta, m) \cdot \text{sn}(\xi, m_1) \cdot \text{cn}(\xi, m_1)}{\text{sn}(\eta, m) \cdot \text{dn}(\xi, m_1)} \right\}$$

$$m = k^2$$

$$m_1 = 1 - k^2$$

with K , the complete elliptic integral of the first kind for $m, K(m)$ and

$$K' = \int_1^{1/k} \frac{dt}{\sqrt{(t^2 - 1)} \sqrt{1 - k^2 t^2}} = K(m_1)$$

The specified geometric parameters of chord, stagger angle and blade spacing are sufficient to perform the analytical transformations described by equations (1). After computing K and K' for a blade spacing of $s = 2\pi$ and for zero stagger, values of n and ξ are then selected at equal intervals (or at weighted intervals if the grid is to be dense near the body or at the trailing edge). Tables of (x,y) for corresponding (ξ,n) points are generated using equations (1). In the Cartesian plane this gives an orthogonal coordinate system about a cascade of flat plates at zero stagger. An example is shown in figure 2. From this, the conformal transformation to a circle is (4),

$$z = x + iy = \frac{s}{2\pi} \left[e^{-i\lambda} \ln \left(\frac{\xi + R}{\xi - R} \right) + e^{i\lambda} \ln \left(\frac{\xi + 1/R}{\xi - 1/R} \right) \right] \quad (2)$$

where $\xi = \delta + i\epsilon$ in the circle plane, and the stagger, λ , is zero.

Equation (2) is easily inverted to obtain (δ,ϵ) tables if

$$\lambda = 0$$

$$s = 2\pi$$

which was the justification for the original calculation of K and K' noted above. The parameter R in equation (2) represents the locations of the upstream and downstream infinity points in the conformal plane. It is a function of cascade solidity (c/s) and stagger angle and can be interpolated from information in reference 4 for the specified values of stagger and spacing. This same R is used in calculating (δ,ϵ) for the zero stagger transform.

The resulting circle is then rotated by applying the exponential terms with the correct stagger and desired spacing, s , to equation (2). The calculated values of z in the Cartesian plane then give an orthogonal grid about a flat plate cascade at the desired stagger angle and solidity. Figure 3 is an example of such a mesh.

The final step in generating this computational mesh is the adjustment of the flat plate grid so that the innermost ellipse coincides with the specified blade shape. This is accomplished by performing a straightforward Newton iteration along each line of constant ξ which intersects the flat plate. The three unknowns to be determined at the intersection of each ξ -line and the body are x , y , and η . The three equations required are equations (1) and

$$y = F(x)$$

where F is a tabular function giving the specified body shape.

A successful iteration yields $(x,y)_{\text{body}}$ and η_{body} where

$$0 < \eta_{\text{body}} < K$$

for most blade surfaces, or

$$0 < K < \eta_{\text{body}}$$

for the pressure surface of blades whose chordline lies outside the blade. The coordinates $(x,y)_{\text{body}}$ replace the point on the flat plate where the ξ -line ended. All other grid points on this ξ -line are shifted by means of a simple linear stretching function that reflects the revised length of the ξ -line:

$$x_i = \frac{K - \frac{\eta_{\text{body}}}{K} \cdot \eta_i}{K - \eta_i} (x_i - x_{\text{plate}}) + x_{\text{plate}} \quad (3)$$

and similarly for each y_i . Completed grids are seen in figures 4 and 5 for several typical blade shapes. This mesh generation scheme has no problem with larger stagger angles ($\approx 75^\circ$) nor with high solidities. Cases with $c/s = 1.45$ have been attempted with good results. However, if the turning angle or camber of the blade is high, while at the same time, stagger and solidity are near the limits mentioned above, the grid lines may become crowded on the suction surface. This is common for turbine blade geometries.

Electrostatic Analog

An Electrostatic Analog has been developed to generate body-fitted orthogonal grids for cascades of large turning thickness and solidity. The development of this grid generation scheme begins by considering the potential field generated by an infinite spacial array of point charges in free space. The density of the charges is assumed to alternate between plus and minus one. The mathematical expression for this field is given by

$$\mathcal{X}(z - z_0) = \sum_{n=-\infty}^{\infty} (-1)^n \ln(z - z_0 - ins) \quad (4)$$

where $\mathcal{X}(z - z_0)$ is the complex potential, $z = x + iy$, z_0 the location of the 0th charge, $i = \sqrt{-1}$, and s the distance between charges.

Equation (4) can be evaluated in closed form by utilizing the theory of calculations of residues (ref. 5). The result is

$$\mathcal{X}(z - z_0) = \sum_{n=-\infty}^{\infty} (-1)^n \ln(z - z_0 - ins) = \ln \tanh \frac{(z - z_0)^\pi}{2s} \quad (5)$$

(Note that this expression is periodic in y with period $2s$.) The potential field generated by distributing these fundamental solutions over the surface of an airfoil in the cascade is given by the integral

$$\psi(z) = \int_L \gamma(z_0) \mathcal{K}(z - z_0) dz_0 \quad (6)$$

where $\gamma(z_0)$ is the yet unknown source density distribution. On the surface of the airfoil (i.e., $z \in L$) the real part of ψ , ζ , will be set equal to one,

$$\text{Real } \psi(z) = 1 \quad z \in L \quad (7)$$

At large distances upstream and downstream of the cascade $\zeta(z)$ is assumed to approach zero. This far-field condition imposes the requirement that

$$\text{Im} \int_L \gamma(z_0) dz_0 = 0 \quad (8)$$

Equation (6) evaluated on the airfoil surface in conjunction with equations (7) and (8) form the integral equation

$$1 = \text{Real} \left\{ \int_L \gamma(z_0) \mathcal{K}(z - z_0) dz_0 \right\}, \quad z \in L$$

$$0 = \text{Im} \int_L \gamma(z_0) dz_0 \quad (9)$$

for the source density function. Once γ is known, the entire potential field can in theory be computed by direct integration of equation (6).

Equation (9) is a singular integral equation, which can be solved by paneling procedures similar to those used in solving potential flow problems. To employ these procedures one must first factor out of the integral equation its singular behavior. For this problem the factor form of equation (9) is

$$1 = \text{Real} \left\{ \int_L \gamma(z_0) \ln \frac{(z - z_0)}{2s} dz_0 + \int_L \gamma(z_0) \ln \frac{2s}{(z - z_0)^\pi} \tanh \frac{(z - z_0)^\pi}{2s} dz_0 \right\} \quad (10)$$

Next the airfoil surface is divided into a series of line segments. Over each of these segments $\gamma(z_0)$ and $\ln[2s/(z - z_0)^\pi] \tanh[(z - z_0)^\pi/2s]$ are approximated by their value at the midpoint of the segment. The singular part of equation (10) is thus approximated as

$$\int_{z_a}^{z_b} \gamma(z_0) \ln \frac{(z - z_0)}{2s} dz_0 = \gamma\left(\frac{z_b + z_a}{2}\right) \left[(z - z_b) \ln \frac{(z - z_b)^\pi}{2s} - (z - z_a) \ln \frac{(z - z_a)^\pi}{2s} \right] \quad (11)$$

with the regular part approximated by

$$\int_{z_a}^{z_b} \gamma(z_0) \ln \frac{2s}{(z - z_0)^\pi} \tanh \frac{(z - z_0)^\pi}{2s} dz_0 \approx \gamma(z_0) (z_b - z_a) \ln \frac{2s}{(z - z_0)^\pi} \tanh \frac{(z - z_0)^\pi}{2s} \Bigg|_{z_0 = \frac{z_b + z_a}{2}} \quad (12)$$

The auxiliary condition is approximated by

$$\operatorname{Im} \int_{z_a}^{z_b} \gamma(z_0) dz_0 \approx \operatorname{Im} \left\{ \gamma \frac{z_b + z_a}{2} (z_b - z_a) \right\} \quad (13)$$

Introducing equations (11), (12), and (13) into (10) and restricting the value of z to the mid-point of each line segment leads to a system of linear algebraic equations for the source density distribution. The solution of these equations can be obtained by standard matrix methods. With γ known, the complex potential field surrounding the cascade can be determined from equation (6). The real part, η and the imaginary part, ξ of this field form a periodic orthogonal body-fitted coordinate system. A typical coordinate system is shown in figure 6. The contours $\eta = \text{constant}$ enclose the airfoil, while the curves $\xi = \text{constant}$ project from the airfoil to the periodic boundary $\eta = 0$. The line extending to upstream and downstream infinity are $\xi = \pm L$, and $\xi = 0$, respectively.

Presently this grid generation scheme utilizes the direct integration procedure outlined above for constructing the bounding curvilinear coordinate. For the other grid lines, on the interior of the mesh, however, the direct procedure proved to be inefficient because of slow convergence. To overcome this difficulty an inverse procedure was developed in which ξ, η become the independent variables and x, y the dependent variables. This inverse procedure is constructed by first noting that the field conversion for the electrostatic potential and flux is the Laplace equation

$$\nabla^2 \xi = 0, \nabla^2 \eta = 0 \quad (14)$$

Inverting these equation yields

$$\left. \begin{aligned} \frac{\partial^2 x}{\partial \xi^2} + \frac{\partial^2 x}{\partial \eta^2} &= 0 \\ \frac{\partial^2 y}{\partial \xi^2} + \frac{\partial^2 y}{\partial \eta^2} &= 0 \end{aligned} \right\} \quad (15)$$

as the governing equations for the inverse mapping (i.e., $x = x(\xi, \eta)$, $y = y(\xi, \eta)$).

The solution of the field equation (15) subjected to boundary conditions consistent with the coordinates of the bounding curvilinear curves yields the desired interior coordinate curves. A second sample grid for a highly combined thick turbine blade generated by the above procedure is shown in figure 7. It is seen that the grid is highly regular with clustering of grid points in regions of rapid flow variations. The periodicity of the grid is quite apparent and leads to simple numerical approximation of flow variables in the neighborhood of the periodic boundary. Flow computations applying this grid generation procedure are presented later in the paper.

SOLUTION METHOD

Governing Equations

The equation to be solved is the 2-D steady, compressible full-potential equation in its conservative form

$$(\rho\phi_x)_x + (\rho\phi_y)_y = 0$$

Similar to the approach taken by several others (7, 12), this equation is to be written at the finite volume element which surrounds each grid point.

With superscript n referring to the artificial time step, a typical formulation at each grid location (i, j) is

with,

$$\phi_{i,j}^{n+1} = \phi_{i,j}^n + \omega \delta \phi_{i,j}^n \quad (16)$$

then

$$L(\phi^{n+1}) = (\rho \phi_x^{n+1})_x + (\rho \phi_y^{n+1})_y = 0 = L(\phi^n) + L(\omega \delta \phi^n) = \nabla(\rho \phi^n) + \omega L(\delta \phi^n) \quad (17)$$

or

$$L(\delta \phi_{i,j}^n) = -\nabla(\rho \phi^n)_{i,j} = -\frac{R_{i,j}}{V_{i,j}}$$

where $V_{i,j}$ is the volume of the local element, ω is the over-relaxation parameter, $\delta \phi_{i,j}^n$ is the unknown change in the local potential field and $R_{i,j}$ is the residual net mass flow out of the finite volume surrounding the grid point. Expanding equation (17) in finite difference form:

$$L(\delta \phi_{i,j}^n) = \frac{\rho_{i+1/2,j}^n \left(\frac{\delta \phi_{i+1,j}^{n-1} - \delta \phi_{i,j}^n}{X_{i+1,j} - X_{i,j}} \right) - \rho_{i-1/2,j}^n \left(\frac{\delta \phi_{i,j}^n - \delta \phi_{i-1,j}^n}{X_{i,j} - X_{i-1,j}} \right)}{X_{i+1/2,j} - X_{i-1/2,j}} + \frac{\rho_{i,j+1/2}^n \left(\frac{\delta \phi_{i,j+1}^n - \delta \phi_{i,j}^n}{Y_{i,j+1} - Y_{i,j}} \right) - \rho_{i,j-1/2}^n \left(\frac{\delta \phi_{i,j}^n - \delta \phi_{i,j-1}^n}{Y_{i,j} - Y_{i,j-1}} \right)}{Y_{i,j+1/2} - Y_{i,j-1/2}} = -\frac{R_{i,j}}{V_{i,j}} \quad (18)$$

Each volume element is defined by the four surfaces parallel to and located halfway between neighboring grid lines as shown in figure 8. The thickness of the element (i.e., relative local streamtube height) is obtained from a specified height distribution or is set to unity for strict two-dimensional flow. Variations in the radial (spanwise) position, r , of the streamtube are accounted for by scaling all tangential re coordinates, (y) with a ratio of local radius, r , to a given upstream radius, r_{∞} . Then, over the area, A_E defined by the four surfaces of the volume element

$$R_{i,j} = \int_{A_E} \rho \bar{u} \, dA = \sum \left(\rho_{i\pm 1/2,j}^n \bar{u}_{i\pm 1/2,j}^n \ell_{i\pm 1/2,j} h_{i\pm 1/2,j} \right. \\ \left. + \rho_{i,j\pm 1/2}^n \bar{u}_{i,j\pm 1/2}^n \ell_{i,j\pm 1/2} h_{i,j\pm 1/2} \right) \quad (19)$$

where h is the local streamtube height normalized to unity far upstream. The velocities, \bar{u} , are normal to the element boundaries and located at the boundaries. Velocity, \bar{u} , and density, ρ , are calculated using the values of potential at the previous iteration.

Using equation (17) and isolating all unknown potential corrections on the left-hand side, equation (18) can be expressed in the form

$$A_{i,j+1} \delta\phi_{i,j+1}^n + A_{i,j} \delta\phi_{i,j}^n + A_{i,j-1} \delta\phi_{i,j-1}^n = \mathcal{R}_{i,j}^n \quad (20)$$

where

$$\mathcal{R}_{i,j} = R_{i,j} + G(\phi^n, \rho^n, \delta\phi_{i-1}^n) \quad (21)$$

and the coefficients

$$A = A(\rho^n, \Delta\xi, \Delta\eta) \quad (22)$$

By writing equation (20) for each point on a grid line of constant ξ ($j = 1, J$) a tridiagonal matrix system is formed which is then solved by the standard Thomas algorithm (ref. 6) for the potential corrections $\delta\phi^n$. New values of the field potential are obtained using equation (16) after all lines are solved ($i = 1, I$).

Sweep Strategy

The grid lines are solved in order beginning with the line which goes to downstream infinity and then proceeding clockwise around the blade shape. This order results in a solution which sweeps against the flow direction on the bottom (pressure) surface of a compressor blade at positive

incidence, where the flow is more likely to be subcritical. This minimizes the chances of sweeping against a supersonic flowfield. It became evident, when symmetric supersonic flows were successfully solved, that direction of sweep is not critical. The apparent reason is that additional damping is applied by the elliptic-like nature of the artificial density used in combination with the sweep strategy. More detail on this effect is described in the next section.

Artificial Density

In equation (18), there is no explicit artificial viscosity term necessary for stability in supercritical flow regions and for smearing shock jumps. As suggested by Hafez, et al. (ref. 1), an implicit viscosity term is incorporated in the density. This modified density is used instead of the physical density in equation (18). The form of the modification is (1)

$$\tilde{\rho} = \rho - \mu \rho_S \Delta S \quad (23)$$

where μ is the switching function to eliminate the density modification in subsonic regions ($M < 1$)

$$\mu = \max\left(0, 1 - \frac{1}{M^2}\right) \quad (24)$$

and $\rho_S \Delta S$ is the total differential component of the density in the flow direction, S , defined by the contravariant velocity components a and b .

Then:

$$\mu \rho_S \Delta S = \mu_a \frac{a}{q} \rho_n \Delta \eta + \mu_b \frac{b}{q} \rho_\xi \Delta \xi \quad (25)$$

where,

$$q = \sqrt{u^2 + v^2}$$

The switching function was split into two terms so that the effect of each component of the density change could be even more efficiently gauged in areas of high flow gradient. In addition, an upwind averaged Mach number was used:

$$\left. \begin{aligned} \mu_a &= \max \left(0, 1 - \frac{i}{M_{av_a}^2} \right), \text{ where } M_{av_a} = \frac{1}{2} (M_{i+1/2,j} + M_{i+1/2,j\pm 1}) \\ \mu_b &= \max \left(0, 1 - \frac{1}{M_{av_b}^2} \right), \text{ where } M_{av_b} = \frac{1}{2} (M_{i+1/2,j} + M_{i+1/2\pm 1,j}) \end{aligned} \right\} (2b)$$

Similarly, Upwind differencing is used for approximating ρ_z and ρ_n . The physical densities used to calculate ρ_z and ρ_n are updated as each line is reached. Implicit in this arrangement is the creation of a timelike cross derivative of density, ρ_{st} , when sweeping against the flow direction. This is because the density at the current line has been calculated using the values of potential and velocity at the latest iteration (i.e., artificial time step), while the values at the next upstream line, where the upwind differences are formed, remain at the previous time step until it in turn is solved. However, when sweeping with the flow, the upstream line from which the density gradients are formed has already been solved and updated. Thus this additional damping due to the time lag of densities is not present when solving with the flow and the artificial compressibility reduces to the original space-lag only.

Boundary Conditions

The boundary conditions applied to the solution system include a specified upstream axial mass flow in the form of an oncoming Mach number, plus incidence and stagger angles. Using global continuity,

$$\rho_{+\infty} u_{+\infty} A_{+\infty} = \rho_{-\infty} u_{-\infty} A_{-\infty} \quad (27)$$

where A is the flow area normal to the streamtube.

The specified flow angle at downstream infinity together with a simple iteration procedure on the isentropic density ratio gives the downstream Mach number boundary condition. For a stagger angle, λ , and upstream incidence (chordwise) of $\alpha_{-\infty}$, equation (27) can be rearranged to yield

$$M_{\infty} \left(\frac{1}{1 + \frac{\gamma-1}{2} M_{\infty}^2} \right)^{\frac{\gamma+1}{2(\gamma-1)}} = F(M_{\infty}) = \frac{A_{-\infty} \cos \beta_{-\infty}}{A_{+\infty} \cos \beta_{+\infty}} M_{-\infty} \left(\frac{1}{1 + \frac{\gamma-1}{2} M_{-\infty}^2} \right)^{\frac{\gamma+1}{2(\gamma-1)}} \quad (28)$$

where

$$\beta = \alpha + \lambda$$

Using a straightforward Newton iteration on equation (28) yields M_{∞} . From this the relative speed ratio is available as:

$$\frac{q_{\infty}}{q_{-\infty}} = \frac{M_{\infty} a_{\infty}}{M_{-\infty} a_{-\infty}} = \left(\frac{1 + \frac{2}{\gamma-1} M_{-\infty}^2}{1 + \frac{2}{\gamma-1} M_{\infty}^2} \right)^{1/2} \quad (29)$$

Periodicity is maintained in the tangential (y) direction by enforcing the relation

$$\phi(x, y + s) = \phi(x, y) + C \quad (30)$$

where s is the blade spacing and

$$C = \oint_{(x,y)}^{(x,y+s)} \mathbf{v} \cdot d\hat{\mathbf{l}} = v_{-\infty} s_{-\infty} \quad (31)$$

On the grid line defining the body, a standard zero normal flow condition is imposed

$$\nabla \phi \cdot \hat{\mathbf{n}} = 0 \quad (32)$$

RESULTS

Some results obtained from these methods are shown in figures 9 through 21. Verification of the code at low speed is provided in figure 9 by the comparison to the methods of Caughey (ref. 7) for the NACA0012 blade shape. The transonic nonlifting case is shown in figure 10 for this same blade. The shock strength and location agree well with similar results using the methods of reference 7. The solution is surprisingly symmetric, particularly in light of the fact that the solution on the lower surface was obtained by marching against the supersonic flow and the upper surface was obtained by marching with the flow. This relative shift in marching direction occurs because the solver was written such that it makes one continuous clockwise sweep of all grid lines around the airfoil. Thus there is a primary difference between this method and other transonic techniques. It is apparently insensitive to the relative direction of the supersonic flow. For the cases tested thus far, this insensitivity to flow direction does not seem to be affected by mesh size (down to $\Delta x = 2$ percent chord). The symmetry of the solution can be seen very effectively in the isonach map of figure 11.

The sensitivity of the system to a near-shock condition can be seen in the results for the supercritical blade shown in figure 12. This is a compressor stator tip section designed for NASA-Lewis by Sanz using a method based on Bauer, et al. (ref. 8). The trailing edge ends in a cusp. The fast recompression is captured well without any over-reaction or steepening into a shock.

The capability to approximate moderate 3-D streamtube effects is demonstrated in figure 13 where both the strict 2-D flow and quasi-3-D flow, as corrected for a given streamtube convergence profile, are compared for

the double circular arc stator of figure 5. Agreement is excellent with results using the method of reference 9. For this case there was a 7-percent gradual contraction in the streamtube from far upstream to far downstream. In addition, the streamtube varied its position along the span (radial shift) by 0.7 percent over the same distance, a negligible effect. The resulting isomach map is shown in figure 14.

A comparison of results for a typical turbine blade section is shown in figure 15. The blade used is designated as the AACE(II) airfoil by R. A. Delaney, to whom we are grateful for supplying the coordinates and experimental data (ref. 10). Agreement is good on the pressure side, but the calculated envelope is slightly low on the suction surface. This is consistent with the metal blade coordinates used in this inviscid calculation. If a suitable boundary layer analysis were included and displacement thickness added to the profile, the suction surface calculation would more accurately match the experimental data. The location of each peak in speed is predicted accurately, even near the trailing edge, despite the inherent difficulty for potential flow methods to go around sharp bends at high velocity without some artificial limitation on calculated speeds. Such limits were not necessary for the coarse mesh used for figure 15 (26 points around the blade). However, finer meshes were unsuccessful without some artificial barrier imposed on Mach number.

Figure 15 also gives an interesting comparison between the two mesh generators described earlier. The results for both grids are virtually identical in the subsonic region as would be expected. In the high-speed region, the exact-orthogonal mesh (electrostatic analog) appears to be slightly more conservative overall than the near-orthogonal grid. Subsequent experience with other denser meshes showed that the

exact-orthogonal mesh provided more stability in high gradient areas, such as the trailing edge. Figures 16 and 17 give views of the two grids used for the calculations of figure 15. An isomach map for the AACE(II) turbine, using the near-orthogonal grid, is shown in figure 18.

As a final example of the importance of streamtube effects on supercritical blade design, figure 19 shows a series of calculations performed on a thick compressor stator hub section developed for NASA-Lewis by Sanz (via ref. 8). The present method was first used to calculate the strict 2-D flow over the blade. This is seen to agree very well with the Sanz hodograph design envelope except at the trailing edge, where the idealized blade of infinite length (hodograph solution) was replaced by a cap of constant radius to connect pressure and suction surfaces for the present method. The remaining two curves are quasi-3-D cases which highlight the effect of changes in spanwise (radial) position of the streamtube. Both cases involve a streamtube thickness change of about -14 percent ($AVDR = 1.15$). The axial distribution of this thickness change (h/h_{∞}) as well as the distribution of spanwise streamtube position (r/r_{∞}) as shown in figure 19 were obtained for this Sanz hub section by using the Katzanis meridional plane computer program (ref. 11). The results are typical for a section near the hub wall with thickness decreasing, and spanwise position increasing about 5 percent. One quasi-3-D case in figure 19 has only the thickness change applied, with radius held constant. The other case has both thickness and radius change. Note that the increasing radial position of the streamtube has a strong decelerating effect on the flow since the blade-to-blade passage now diverges (r_0 larger at trailing edge than at leading edge). A design using this result could tolerate higher blade flow rates than one which ignored these radial effects.

Figure 20 shows the isomach map for the case of thickness variation only. The shock appears as expected near 40 percent chord. Figure 21 is for the case of both thickness and radius variation. Note that the shock has washed out and flow in the passage has decelerated.

CONCLUSIONS

A reliable method has been presented for calculating the flowfield about a cascade of arbitrary 2-D airfoils which can be made to approximate the three-dimensional flow in a turbomachinery blade row by correcting for streamtube convergence and radius shift. The method is a fully conservative solution of the full potential flow equation using a body-fitted periodic mesh, with an artificial density imposed in the transonic region to insure the capture of shock waves. A computer code has been developed using the methods described above. It has been tested using a variety of turbomachinery and general blade profiles. The calculation of a shocked symmetric NACA blade has verified that this method is insensitive to the relative directions of supersonic flow and SLOR sweep. Comparison of results for several well-known supercritical blades has shown satisfactory agreement with their hodograph solutions. The approximation of moderate 3-D streamtube effects was demonstrated by a good comparison between this method and results using the Katsanis code on a DCA compressor stator. 2-D and quasi-3-D calculations for a supercritical compressor stator indicated that the moderate 3-D effects included in this method are important enough to radically affect design considerations in high-speed regions of the blade. These results all indicate that the method described is a useful one for analyzing off-design performance of turbomachinery blading.

APPENDIX A

LIST OF SYMBOLS

- A (eqs. (20)(22)) variable coefficient of change in potential for field equation
- (eqs. (27)(28)) flow area normal to the streamchannel direction
- A_E (eq. (19)) total surface area of finite volume element
- a contravariant velocity component (η direction) in computational space
- b contravariant velocity component (ξ direction) in computational space
- C circulation about the airfoil as defined by the given values of flow angle
- c blade chord
- C_x length of passage along x-axis, from leading edge to trailing edge when blade is at setting angle
- F tabular function of body shape (x,y) pairs
- G transposed terms in field equation involving known (previously determined) potential corrections
- h local streamtube height normalized to unity far upstream
- K complete elliptic integral of the first kind for (k^2)

$$\int_0^{\pi/2} dt / \sqrt{1 - k^2 \sin^2 t}$$
- K' complete elliptic integral of the first kind for ($1 - k^2$)
- \mathcal{X} complex electro-static potential field generated by infinite array of point charges
- k $e^{-(\pi c)/(s \cos \lambda)}$ parameter, defined by cascade geometry, for obtaining Jacobian elliptic functions
- L full potential operator (eq. (17))
- l length of bounding surfaces for finite volume (see fig. 8)

M	Mach number
m	k^2
\hat{n}	unit vector, normal to airfoil surface
q	magnitude of flow speed, normalized to unity at far upstream conditions
R	residual net mass flow out of a finite volume using potential values from previous iteration (eq. (19))
\mathcal{R}	$R + G$, total residual right hand side for field equation at each volume
r	local spanwise radial position of streamchannel normalized to unity far upstream
S	flow direction as defined by contravariant velocities a and b in equation (25)
s	blade spacings
T	a combination of Jacobian elliptic functions, defined in equation (1)
u	x-component of velocity in the physical plane
V	total physical velocity vector, $u\hat{i} + v\hat{j}$ (eq. (31))
v	y-component of velocity in the physical plane
x	streamwise position coordinate, i.e., in figure 4 x-axis is horizontal
y	tangential position coordinate, i.e., in figure 4 y-axis is vertical
z	coordinate to transform a physical point to complex plane, $z = x + iy$
z_a	coordinate of beginning of one line segment. Blade is divided into segments in solving for electrostatic analog grid

z_b	coordinate at the end of a segment of the blade surface
z_0	coordinate of zeroth charge for electrostatic analog
α	incidence angle of flow as measured from chordline of blade
β	angle of flow as measured from x-axis
γ	ratio of specific heats
$\gamma(z_0)$	(electrostatic analog grid procedure). Source density distribution defined in equation (1)
ζ	abscissa coordinate in the plane of the conformal circle transformation (interpolation scheme, eq. (2))
$\delta\phi$	change in the local potential field, the unknowns in equation (18)
ϵ	ordinate in conformal transformation plane (eq. (2))
ξ	coordinate in computational space whose contours in physical space radiate from the blade and terminate on the periodic boundary
η	coordinate in computational space whose physical contours surround the airfoil
θ	tangential coordinate in radians, $y = r\theta$
λ	stagger or setting angle of the blade row, as measured from x-axis to chordline
μ	switch function to control the artificial density modification (eq. (24))
π	3.14159265
ρ	physical density
$\bar{\rho}$	artificial density as described in equation (23)
ϕ	flow velocity potential function
ψ	electrostatic potential function due to charge distribution on blade surface (eq. (6))
ω	over-relaxation parameter, $1 < \omega < 2$
Ω	defined in equation (1)

Subscripts:

- i position on computational plane in ξ -direction
- j position on computational plane in η -direction
- x differentiation with respect to streamwise position coordinate, x
- y differentiation with respect to tangential coordinate, y
- ξ differentiation with respect to ξ
- η differentiation with respect to η
- $-\infty$ conditions at far upstream station
- $+\infty$ far downstream conditions

Superscripts:

- n artificial time step (iteration level)
- $-(\bar{\quad})$ (eq. (19) and fig. 8) average over the length, Δ , of the velocity component normal to the element surface along Δ

REFERENCES

1. Hafez, M., South, J., and Murman, E., "Artificial Compressibility Methods for Numerical Solutions of Transonic Full Potential Equation," AIAA Journal-Vol. 17, No. 8, Aug. 1979, pp. 838-844.
2. Ives, D. C. and Liutermoza, J. F., "Analysis of Transonic Cascade Flow Using Conformal Mapping and Relaxation Techniques," AIAA Paper 76-370, July 1976.
3. Jahnke, E. and Emde, F., Tables of Functions with Formulae and Curves, 4th ed. Dover, New York, pp. 92-95.
4. Hawthorne, W. R., ed., Aerodynamics of Turbines and Compressors, Princeton University Press, Princeton, N.J., 1964, pp. 29-31.
5. Fuchs, B. A. and Shabat, B. V., Functions of a Complex Variable and Some of Their Applications, Vol. 1, Pergamon Press, New York, 1961, pp. 183-187.
6. Roache, P. J., Computational Fluid Dynamics, Rev. Printing, Hermosa Publications, Albuquerque, N.M., 1976, pp. 345-347.
7. Caughey, D. A. and Jameson, A., "Numerical Calculation of Transonic Potential Flow About Wing-Fuselage Combinations," AIAA Paper 77-677, June 1977.
8. Bauer, F., Garabedian, P., Korn, D., and Jameson, A., Supercritical Wing Sections II, Lecture Notes in Economics and Mathematical Systems, Vol. 108, Springer-Verlag, New York, 1975.
9. Katsanis, T., "ORTRAV Program for Calculating Transonic Velocities on a Blade-to-Blade Stream Surface of a Turbomachine," NASA TN D-5427, Sept. 1969.

10. Huffman, G. D., McClure, R. B., Holtman, R. L., and Sinnett, G. T.,
"Results of a Two-Dimensional Turbine Cascade Test," Research Note
71-47, Detroit Diesel Allison, Indianapolis, Ind., 1971.
11. Katsanis, T. and McNally, W. D., "Revised FORTRAN Program for Calculating
Velocities and Streamlines on the Hub-Shroud Midchannel Stream Surface
of an Axial-, Radial-, or Mixed-Flow Turbomachine or Annular Duct,"
NASA TN D-8431, July 1977.
12. Caspar, J. R., Hobbs, D. E., and Davis, R. L., "The Calculation of
Potential Flow in Cascades Using Finite Area Techniques," Paper
79-0077, AIAA 17th Aerospace Sciences Meeting, New Orleans, Louisiana,
January 1979.

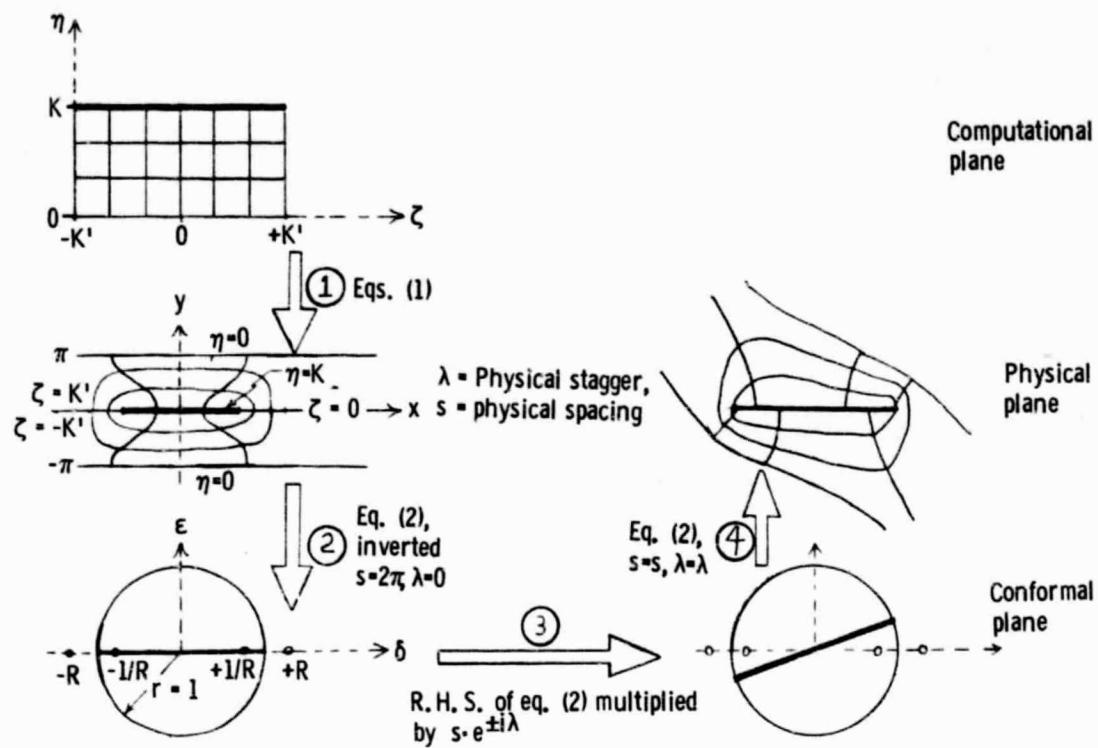


Figure 1(a). - Analytical transformation steps for near-orthogonal grid development.

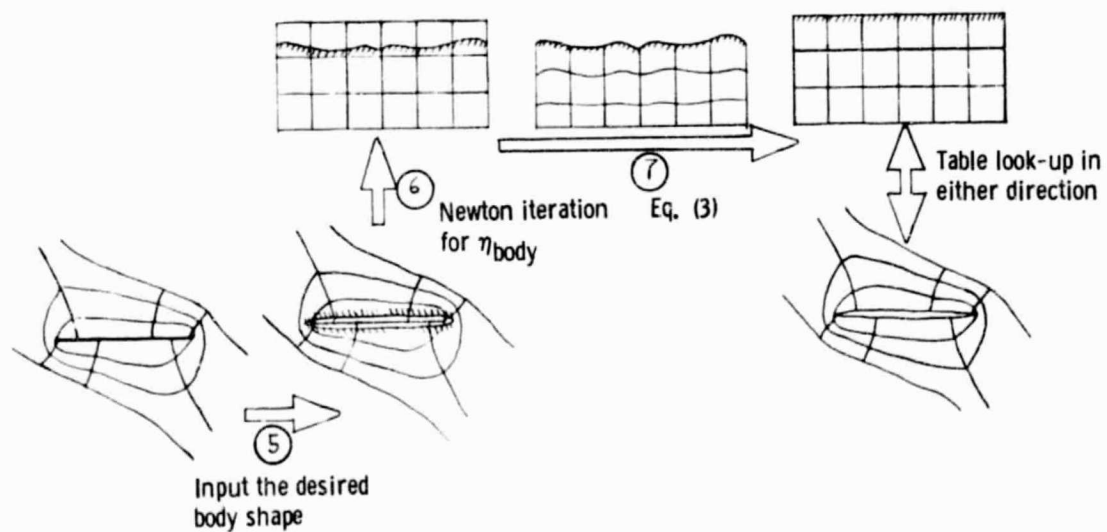


Figure 1(b). - Interpolation and shear transformation steps for near-orthogonal grid development.

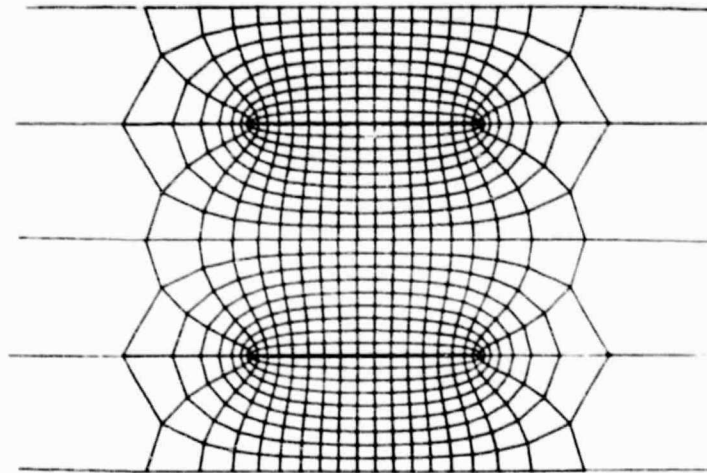


Figure 2. - Flat plate cascade at zero stagger.

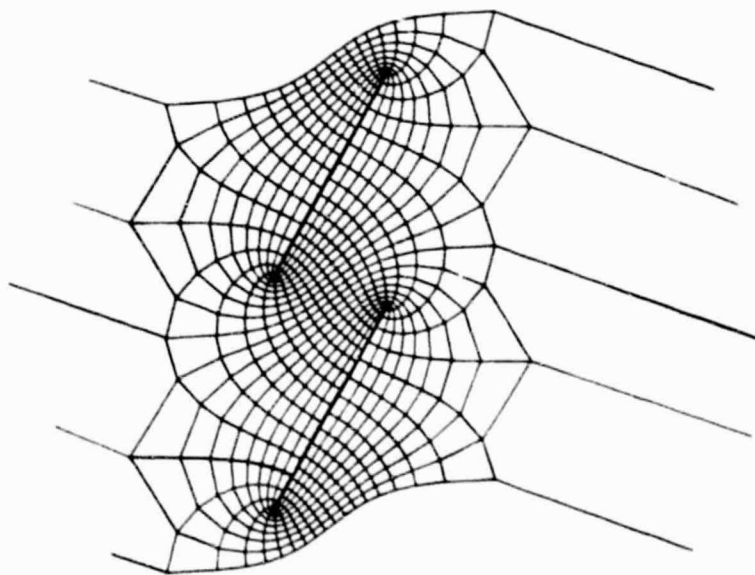


Figure 3. - Flat plate cascade rotated to desired stagger angle.

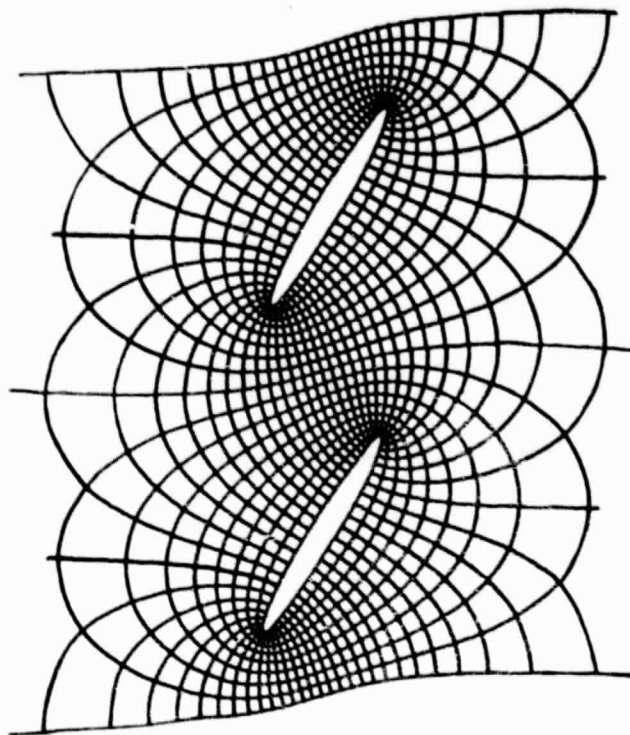


Figure 4. - Near-orthogonal mesh for a symmetric blade.

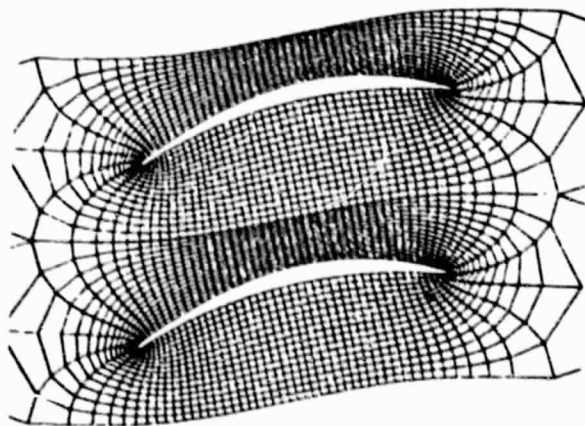


Figure 5. - Near - orthogonal mesh for a double circular arc compressor stator.

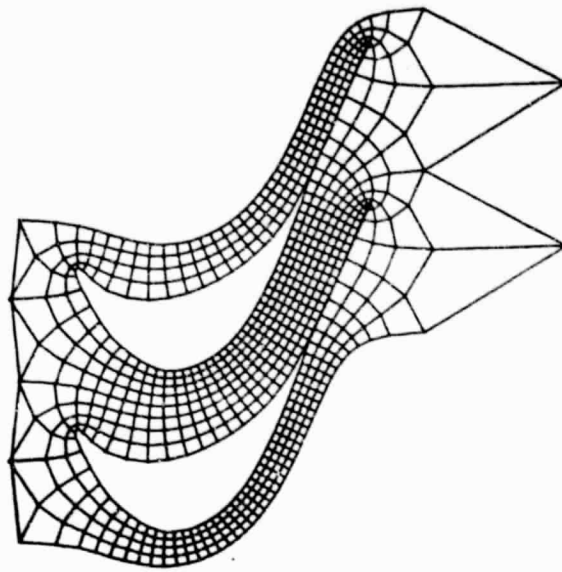


Figure 6. - Typical mesh generated by electro-static analog procedure for a turbine blade with trailing extension.

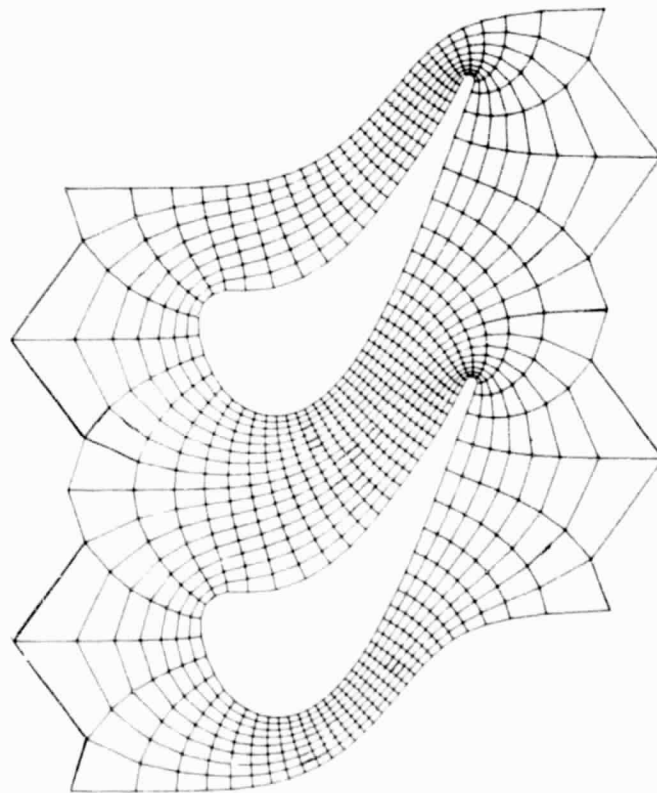


Figure 7. - Computational mesh developed by electrostatic analog procedure for another thick turbine blade.

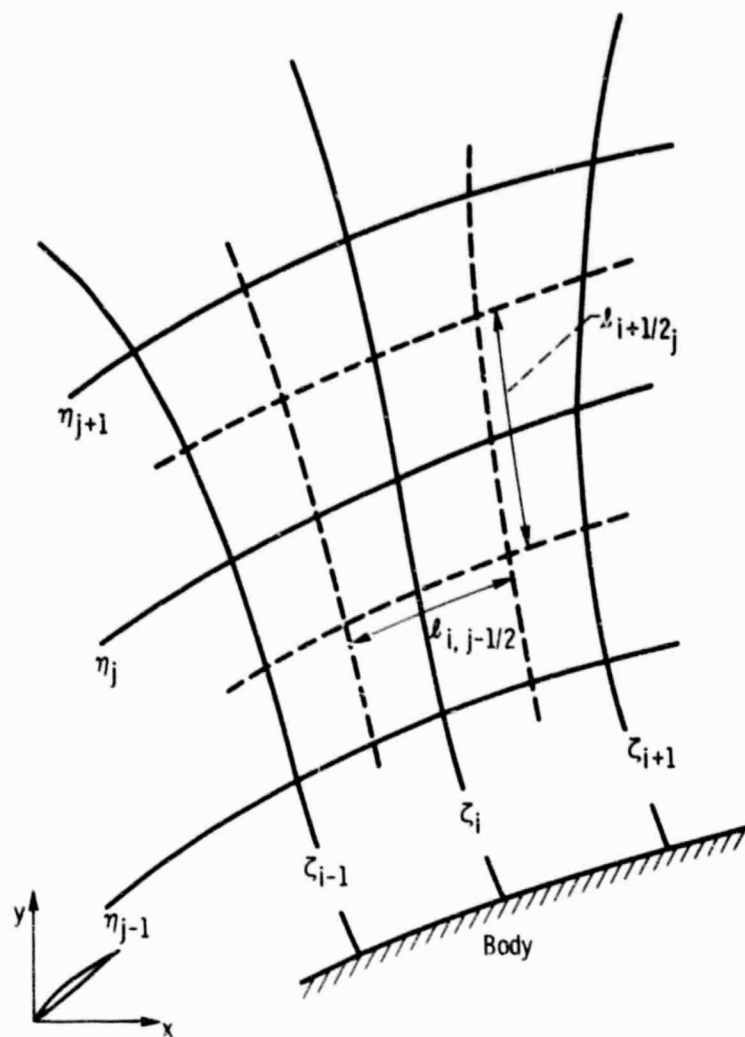


Figure 8. - Finite volume element in physical space.

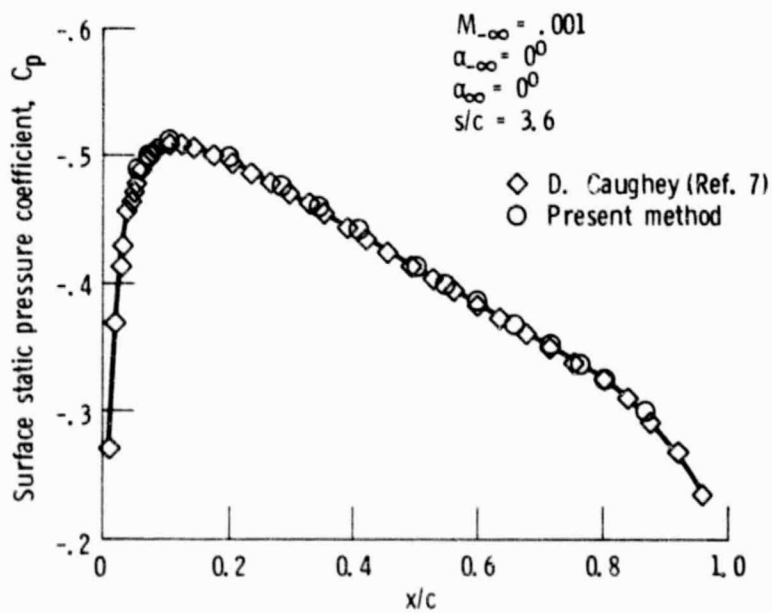


Figure 9. - NACA0012 cascade nonlifiting subsonic results.

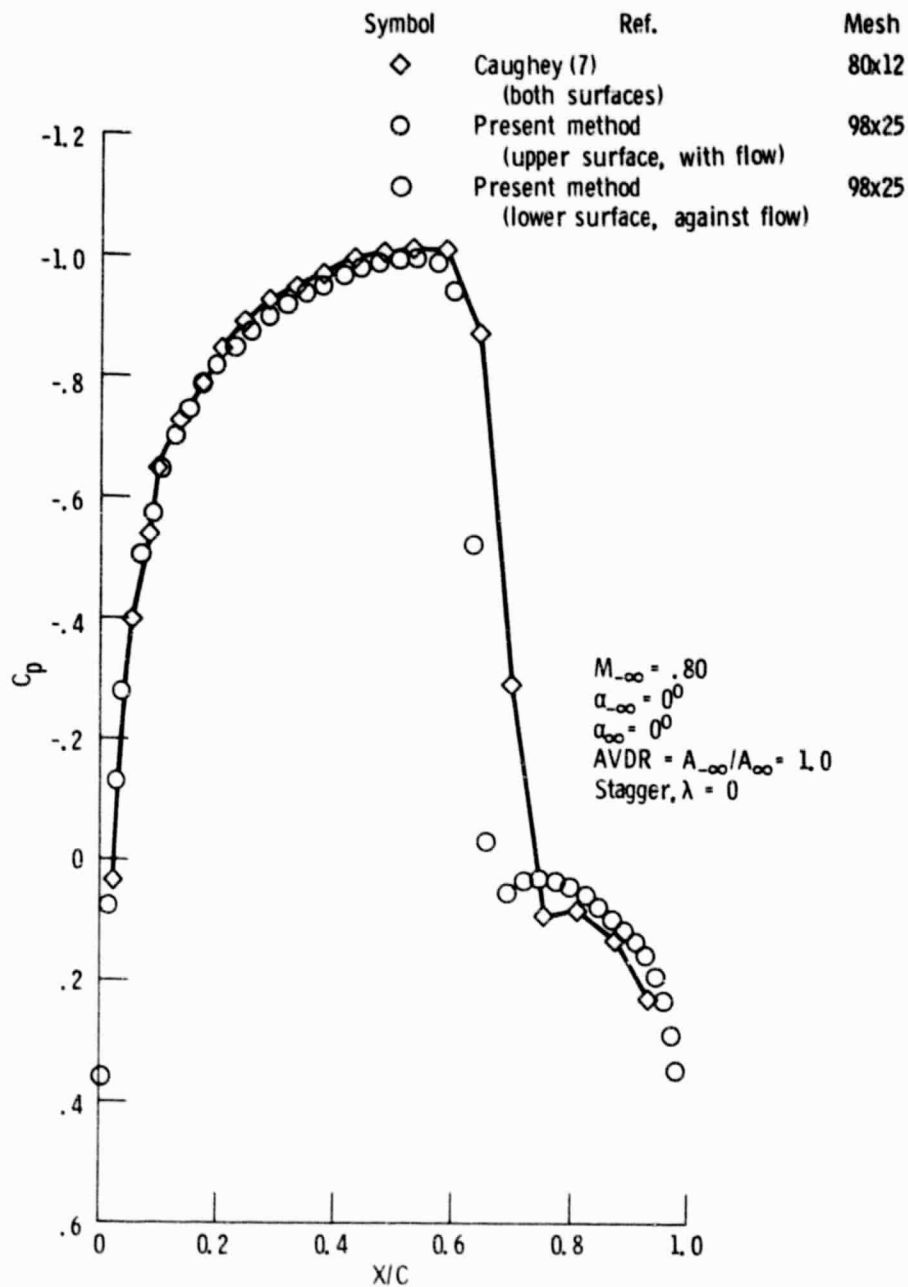


Figure 10. - NACA0012 cascade nonlifting transonic results.

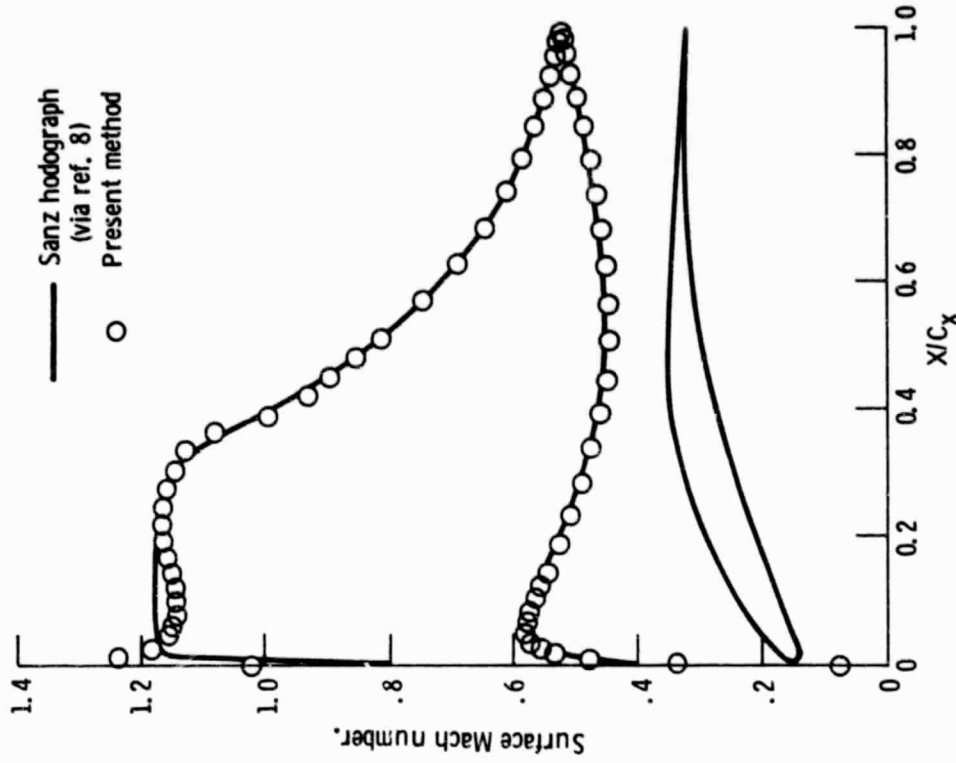


Figure 12. - Sanz supercritical stator tip section.

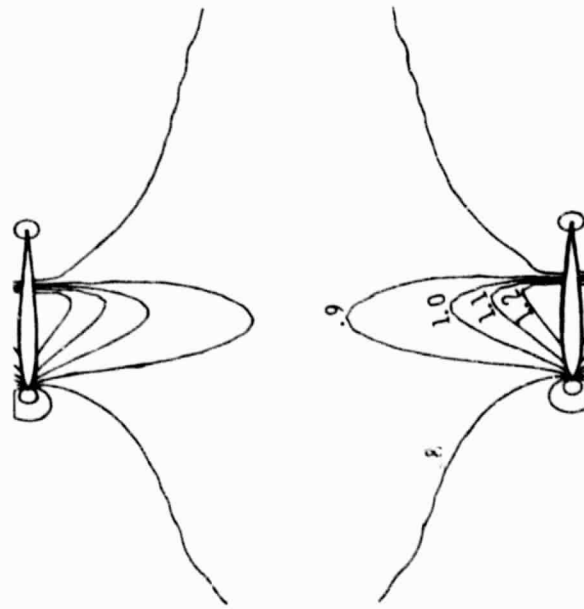


Figure 11. - Isomach map for NACA0012 using present method.

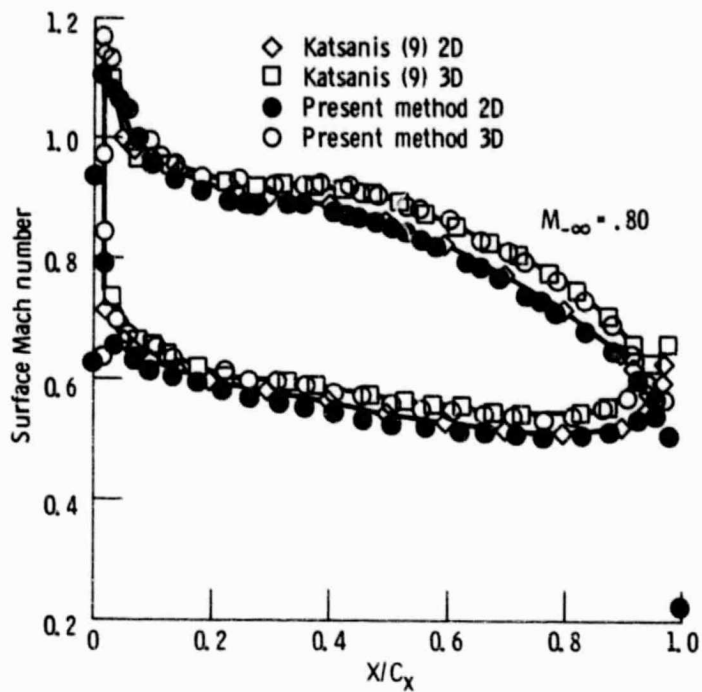


Figure 13. - Comparison of 2D and 3D results for DCA compressor stator.

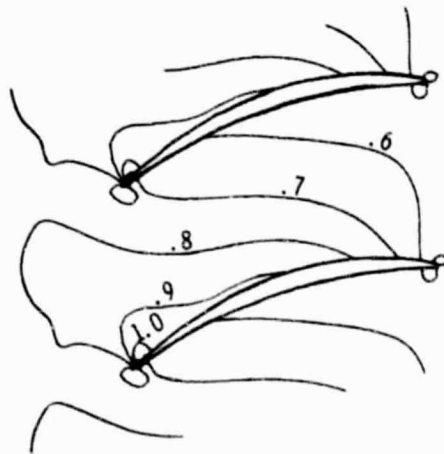


Figure 14. - Isomach map for quasi-3D case of DCA stator using present method.

	M_∞	M_∞	β_∞
◇ DDA Exp. (10)	0.251	.988	66.
□ Present method (near-ortho. grid)	.251	.988	65.
△ Present method (exact ortho. grid)	.251	.988	65.

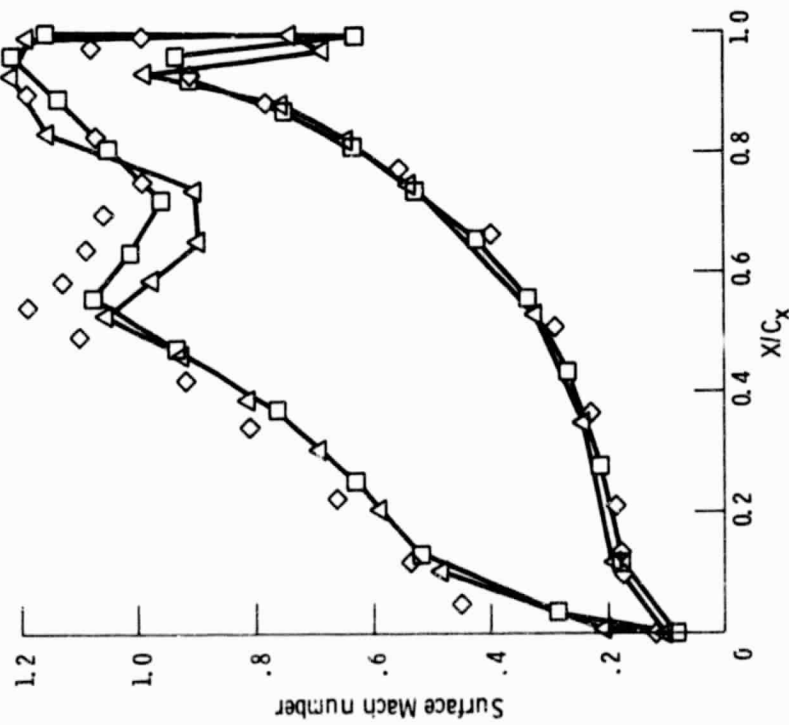


Figure 15. - Comparison of experimental and calculated results for turbine cascade, AACE (II).

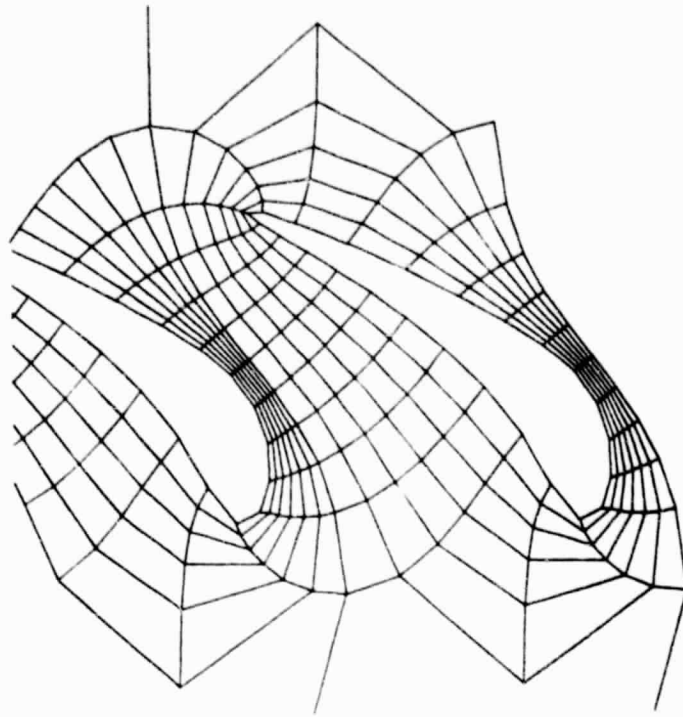


Figure 16. - Near-orthogonal coarse mesh for DDA AACE(II) turbine cascade.

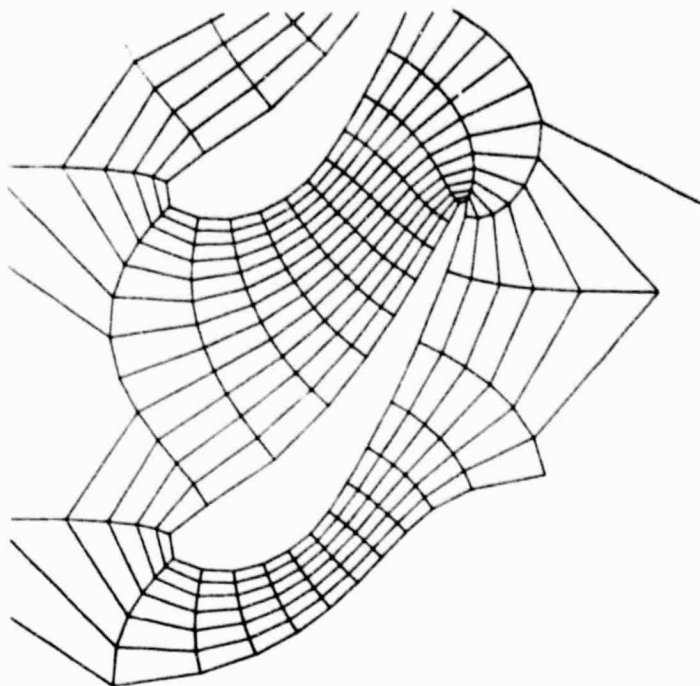


Figure 17. - Exact orthogonal coarse mesh for DDA AACE (II) turbine cascade.

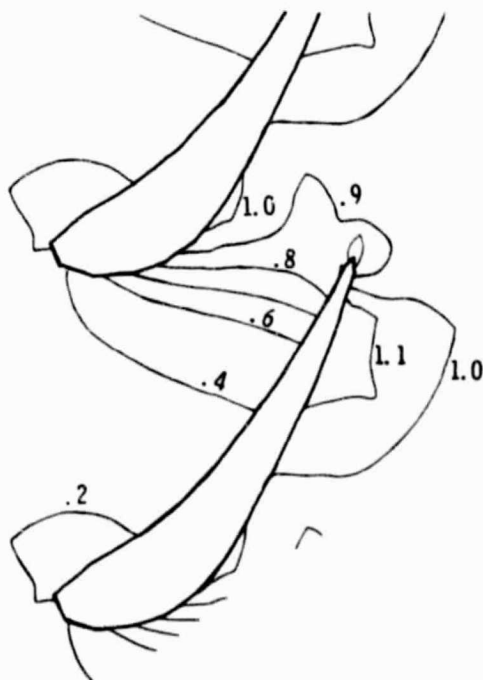


Figure 18. - Isomach map of DDA AACE (II) turbine using the near-orthogonal mesh.

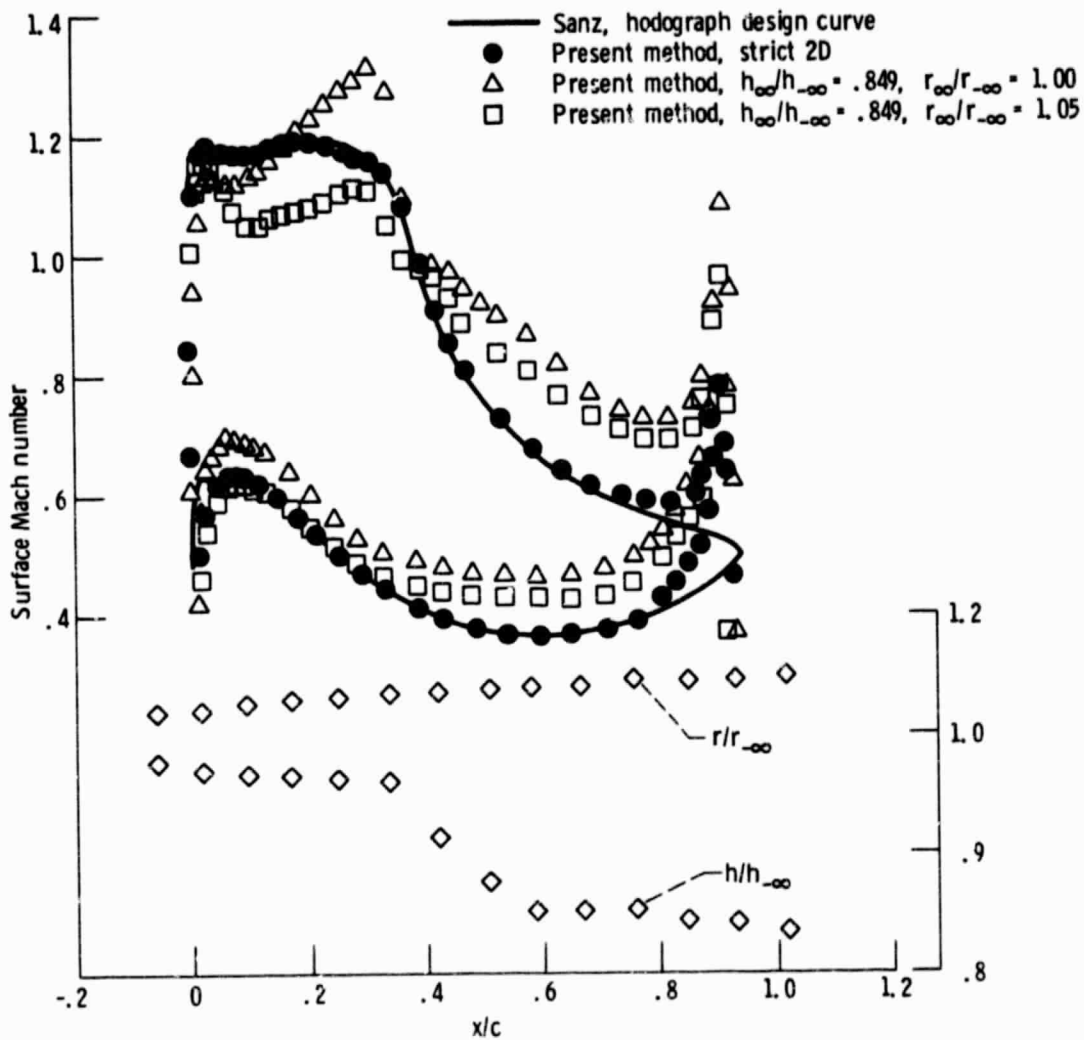


Figure 19. - Effect of streamtube's radial position and thickness on flow about a supercritical compressor stator hub section.

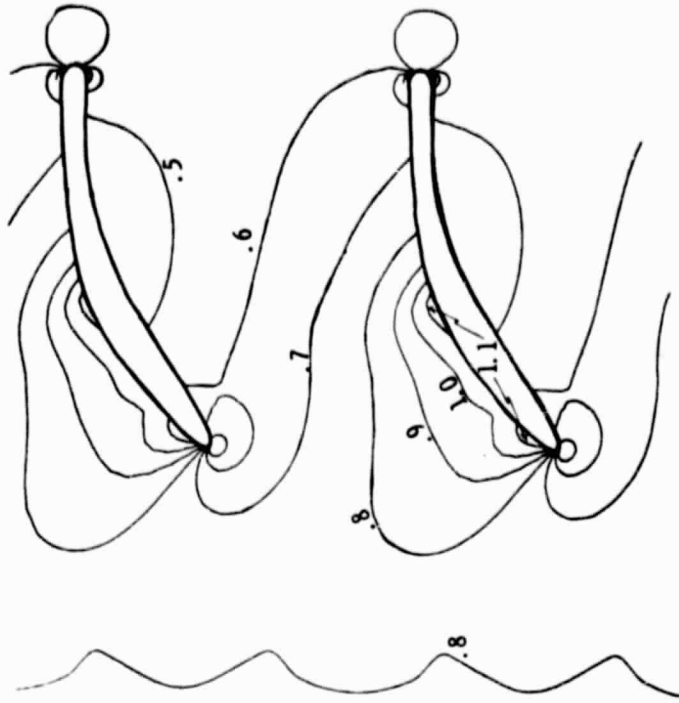


Figure 21. - Isomach map for Sanz stator with streamtube thickness variation and radius variation.

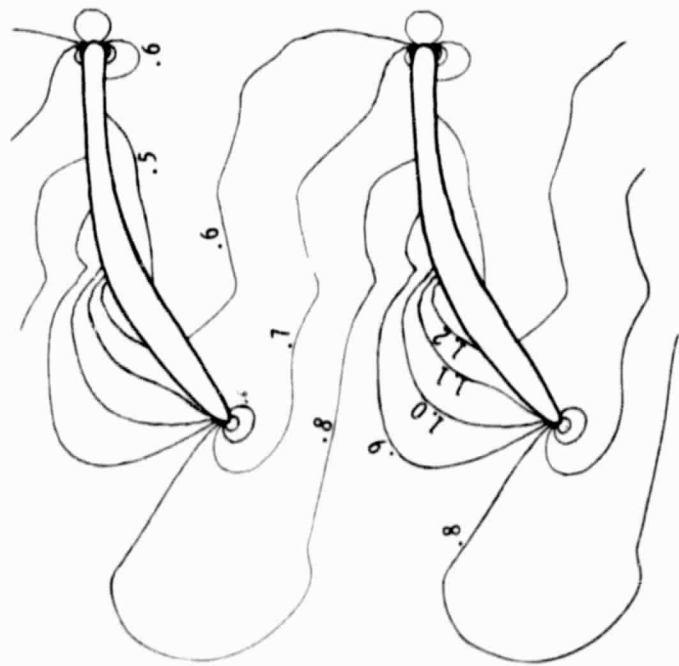


Figure 20. - Isomach map for Sanz stator with streamtube thickness variation and constant radius.